# Development of a High-Fidelity Time-Dependent Aero-Structural Capability for Analysis and Design

Dimitri J. Mavriplis *
Evan Anderson †
Ray S. Fertig III ‡
Mark Garnich §
*Department of Mechanical Engineering, University of Wyoming, Laramie, WY 82071*
Zhi Yang ¶
*Scientific Simulations LLC, Laramie, WY 82072*

**The development of a tightly coupled aeroelastic simulation capability for analysis and design is described in this paper. The method makes use of a well established unstructured mesh computational fluid dynamics solver, combined with a recently developed structural dynamics code. These two disciplinary codes are coupled through a fluid-structure interface and a mesh deformation capability. The discrete adjoint for all disciplinary software components has also been implemented with the goal of enabling time-dependent aeroelastic optimization. The individual disciplinary components are validated both in analysis and adjoint mode. Subsequently, the coupled aeroelastic analysis capability is demonstrated for both static and dynamic problems. Based on the validation and performance of these components, the future development of a time dependent coupled aeroelastic adjoint optimization capability is described.**

## I. Introduction

Over the last decade, Reynolds-averaged Navier-Stokes (RANS) computational fluid dynamics (CFD) methods have become the high-fidelity analysis and design tool of choice in the aerospace industry for fixed and rotary wing aircraft.[1,2] Although single discipline aerodynamic simulations are still most prevalent particularly for fixed wing applications, incorporating fully coupled aeroelastic effects is generally seen as the next step in the drive to higher fidelity analysis and optimization capabilities. This is even the case for steady-state fixed wing problems, as evidenced by the focus of the upcoming sixth Drag Prediction Workshop,[3] which focuses on incorporating static aeroelastic effects. Aeroelastic effects take on added importance for time-dependent problems such as fixed wing flutter problems, and rotorcraft simulations where the structural response and the coupling between fluid and structure plays a dominant role in the overall simulation.

Many aeroelastic simulation capabilities can be classified into two groups: one group that employs high fidelity aerodynamic models (ie. RANS) with simplified structural models (i.e. modal models), and a second group that employs high-fidelity finite element structural models along with simplified aerodynamic models. The premise of the current work is that a modern high-fidelity aeroelastic capability must include both high-fidelity aerodynamic and structural models and these should be solved in a tightly coupled fashion for both steady-state and time-dependent problems.

In addition to the aeroelastic analysis problem, aeroelastic design optimization is increasingly being pursued as designers seek to incorporate higher-fidelity and additional disciplines at earlier stages of the

*Professor, AIAA Associate Fellow; email: mavriplis@uwyo.edu
†PhD Candidate, Member AIAA; email: evanski@uwyo.edu
‡Assistant Professor, Member AIAA; email: fertig@uwyo.edu
§Associate Professor, Senior Member AIAA; email: garnich@uwyo.edu
¶Research Engineer , Member AIAA; email: zyang@scientific-sims.com

design process. Since gradient-based optimization is generally taken to be the most viable approach at high fidelity, adjoint methods are necessary to obtain sensitivities of a single or small number of objectives with respect to large numbers of design parameters at reasonable cost.

The use of adjoint equations is now fairly well established in steady-state aerodynamic shape optimization.[4] Additionally, adjoint methods for coupled aeroelastic or aerostructural optimization have been pursued over the last decade by various contributors.[5–7] On the other hand, only recently have inroads been made into extending adjoint methods to time-dependent problems. Initial demonstration of time-dependent aerodynamic shape optimization has been shown in reference[8] and subsequently extended to airfoil dynamic stall problems,[9] and to simple three-dimensional pitching wing problems.[10] More recently, realistic rotorcraft time-dependent optimization has been performed in references.[11–14] Time-dependent adjoint formulations have also been extended to aerostructural problems, first in two dimensions for a flutter suppression problem,[15] and more recently in three dimensions for flexible helicopter rotor problems.[16–18] However, in the latter case, a simple finite element beam model was used to represent the blade structure, since this approach was simple enough to enable a relatively straight-forward adjoint formulation and efficient parallel solution, while providing realistic non-linear structural dynamics effects, particularly for slender bodies such as rotor blades.

Thus, the next logical step in the drive to higher fidelity aeroelastic effects for both fixed wing and rotary wing problems involves the incorporation of a high-fidelity finite element structural model based on brick and shell elements, as is used in standard aerospace structural design practices. While such models are common in many commercial simulation tools, the need to obtain adjoint-derived sensitivities for the individual contributing disciplines results in the requirement of having complete source code access, since adjoint linearization is an inherently intrusive process. Therefore, the most practical approach consists of developing an in-house structural model that can be tailored for sensitivity analysis.

In this paper, we discuss the development of a coupled aeroelastic analysis and adjoint optimization capability. This is achieved through the development of a high-fidelity finite element structural dynamics solver with adjoint capability, which is coupled with an existing unstructured mesh RANS CFD solver, which itself contains a well validated time-dependent adjoint capability. The focus is on the development and validation of the structural dynamics analysis and adjoint solver, and on the coupling of the two disciplinary codes in a numerically and computationally efficient manner within a large scale parallel computing environment.

## II. Flow Solver

The NSU3D unstructured mesh Reynolds averaged Navier-Stokes (RANS) flow solver is used in this work. NSU3D has been widely validated for both steady-state and time-dependent problems through participation in the Drag Prediction Workshop, High-Lift Prediction Workshop and Aeroelastic Prediction Worskhop series.[1,19–21] The discretization is based on a second-order accurate vertex-centered finite-volume approach, using matrix-based artificial dissipation. NSU3D uses a line-implicit agglomeration multigrid algorithm which can be configured either as a non-linear solver, a linear solver within an approximate Newton method, or as a preconditioner for GMRES for driving the non-linear steady-state residual to zero.[22] For time-dependent problems, these same solvers are reused in a dual-time stepping approach to solve the non-linear problem arising at each time step based on a second-order backward difference time discretization. For periodic and quasi-periodic problems, parallel time-spectral (TS) and BDF-time-spectral (BDFTS) time discretizations have been implemented and demonstrated for rotorcraft applications.[23] NSU3D has also been coupled with a finite-element beam structural model, both for steady state[21] and time dependent problems[18] in analysis and adjoint mode.

In previous work we have spent considerable effort implementing and verifying the discrete adjoint approach for computing exact sensitivities within the NSU3D unstructured mesh RANS CFD solver for steady-state and time dependent problems. The first demonstration of this capability was shown in reference[15] for a simple pitching wing problem, and application to a realistic rotorcraft optimization problem was shown subsequently in reference.[14] This capability has been extended to time-dependent aerostructural optimization problems, through the inclusion of a beam structural model, an unstructured mesh deformation capability, a prescribed blade motion facility, and the corresponding adjoint equations of all these individual disciplinary modules. The comprehensive capability was recently demonstrated for a helicopter rotor in forward flight which involves prescribed cyclic pitching of the blades and trim constraints.[18]

In addition to the time dependent adjoint capability, the forward or tangent sensitivity formulation has

been implemented and a complex version of the entire code is maintained in order to enable verification of the computed adjoint sensitivities to machine precision. As an example, Table 1 illustrates the verification of adjoint computed sensitivities with those obtained using the forward sensitivity approach and by the complex step method[24,25] for the forward flight aeroelastic rotor problem discussed in reference,[18] using a beam structural model and a 2 degree time step. In these results, all equations are converged to machine precision at each time step and a full rotor revolution is simulated (180 time steps). These results demonstrate that exact sensitivities (at least 11 significant digits) can be obtained and preserved over multiple time steps, and that the agreement does not degrade with increasing numbers of time steps.

**Table 1. Adjoint sensitivity verification for Forward Flight**

| n | Uncoupled (Rigid) | Coupled (Aero-elastic) |
|---|---|---|
| 1 (C) | 8.135662924562**930**E-005 | 7.569817143673**123**E-005 |
| (T) | 8.135662924562**923**E-005 | 7.569817143673**061**E-005 |
| (A) | 8.135662924562**884**E-005 | 7.569817143672**761**E-005 |
| 2 (C) | 7.303561433847**516**E-005 | 6.040142774935**852**E-005 |
| (T) | 7.303561433847**498**E-005 | 6.040142774935**835**E-005 |
| (A) | 7.303561433847**042**E-005 | 6.040142774935**570**E-005 |
| 3 (C) | 1.579075715783**277**E-005 | -4.959909870786**381**E-006 |
| (T) | 1.579075715783**178**E-005 | -4.959909870787**765**E-006 |
| (A) | 1.579075715780**985**E-005 | -4.959909870785**228**E-006 |
| 4 (C) | -3.279789405316**752**E-005 | -6.193896187819**846**E-005 |
| (T) | -3.279789405316**760**E-005 | -6.193896187820**087**E-005 |
| (A) | -3.279789405324**491**E-005 | -6.193896187820**419**E-005 |
| 5 (C) | -7.4662642948**60007**E-005 | -1.142069116982**308**E-004 |
| (T) | -7.4662642948**59811**E-005 | -1.142069116982**308**E-004 |
| (A) | -7.4662642948**78836**E-005 | -1.142069116982**432**E-004 |
| 180 (C) | -2.60622548751**0254**E-003 | -5.176189427439**016**E-003 |
| (T) | -2.60622548751**0356**E-003 | -5.176189427439**005**E-003 |
| (A) | -2.60622548752**8119**E-003 | -5.176189427434**507**E-003 |

## III. FEM Formulation

One of the principal objectives of this work is to develop a higher fidelity structural model to replace the beam model used in the previous example with the goal of providing more realistic structural models for fixed and rotary wing configurations. To this end, a finite element based structural model has been developed and tested which supports a subset of the common brick and shell element types encountered in commercial structural analysis codes. The new FEM structural model supports standard tri-linear 8-node brick elements, as well as the corresponding degenerate 6-node wedge (pyramidal) and 4-node tetrahedral elements. Additionally, 8-node incompatible mode elements have been implemented. These element types show significant improvement in accuracy as compared to the original tri-linear formulation, particularly for problems with high bending loads, but remain substantially less computationally expensive compared to the quadratic 20 node hexahedral elements. In addition, two types of shell elements have also been implemented: 3-node triangular shell elements and 4-node quadrilateral shell elements, all illustrated in Figure 1. The governing equations for the structural response are derived from the widely used virtual work formulation.[26]

A design feature of the in-house FEM structural analysis code is that it should be compatible with existing commercial structural analysis software tools such as Abaqus and Nastran. Therefore, the in-house structural solver contains an interface that can directly read in model files generated within Abaqus. Structural models built using other commercial tools such as Nastran can be read into Abaqus and translated to the Abaqus

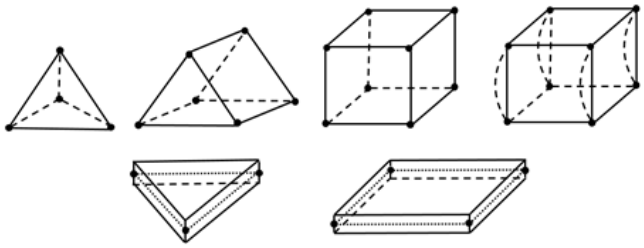

**Figure 1. Illustration of solid and shell finite element types currently implemented in structural dynamics code.**

file format, which in turn can be read in by the in-house code. The implementations of the various supported element types have been verified by performing unit tests on each element type and comparing with analytic solutions when available, and with the equivalent solutions generated by Abaqus. Validation experiments have also been performed on various simple structural models with mixtures of the supported elements by comparing computed stress, strain and deflection results with those produced by Abaqus.

The FEA module features three main types of on-board solvers by which to obtain the structural response, specifically 1) direct solver for sparse matrices via Cholesky factorization, 2) conjugate gradient with optional preconditioning and 3) Q-iteration (through which methods such as Jacobi/Gauss-Seidel can be implemented).[27] To optimize performance, an algorithm to rearrange the global node-ordering and minimize the bandwidth of the linear system was implemented, following the basic algorithm of Sloan.[28] These solvers are all sequential in nature and are used for moderate size structural models which fit on a single processor. For larger structural models that must be run in parallel, currently the MUMPS parallel direct solver is employed.[29] Within the context of a parallel computing environment, the structural analysis code reads in a single or multiple structural models. Each model can reside on a single processor, or be distributed across multiple processors. However, no processor can contain more than one partition of one structural model. Thus, for example, if we are modeling a four-bladed rotor system, each blade must reside on a separate processor and a minimum of four processors is required to run such a case. The in-house code is responsible for building the stiffness matrix for each model, either sequentially or in parallel, and then calls the MUMPS parallel direct solver as a library, which factorizes the matrix and optionally returns a solution vector when provided with a right hand side vector. The MUMPS parallel direct solver has shown good scalability up to several hundred processors, although scalability beyond this level remains under investigation.

For time-dependent problems, the Newmark-Beta implicit method[30] with optional Rayleigh damping[26] as defined by the user has been implemented. The Newmark-Beta method discretizes the second-order differential equation arising from the structural dynamics formulation directly (as opposed to recasting this as a first-order system) and can make use of any of the above direct or iterative solvers at each implicit time step. For purely periodic problems, the time-spectral method has also been implemented for the structural dynamics equations. The time-spectral discretization is also applied directly to the second-order differential equations arising from the structural dynamics. This has been achieved by analytically deriving the time-spectral coefficients for the second derivative term, in addition to the coefficients typically used for the first time derivative term in traditional CFD applications.[31] The time-spectral solver makes use of an approximate factorization scheme[32–34] where the spatial factor is solved using the same direct or iterative solvers described previously. The in-house structural model has been tested on various representative configurations including various brick element solid models, the CRM shell-based wing box model, and a shell-based wind turbine structural model, as depicted in Figure 2.

In order to enable the computation of sensitivities of the structural model with respect to user-defined design variables, the discrete adjoint of the structural model for all element types has been derived, implemented and verified. The forward and adjoint linearization of the structural model discretization with respect to nodal coordinates, material properties and orientations, and shell thickness have been implemented. The sensitivities of the structural response are computed exactly, by direct analytical differentiation of the original source code for the finite element formulation, as opposed to the use of automatic differentiation or finite-differencing, which are more costly and prone to roundoff error in the latter case.

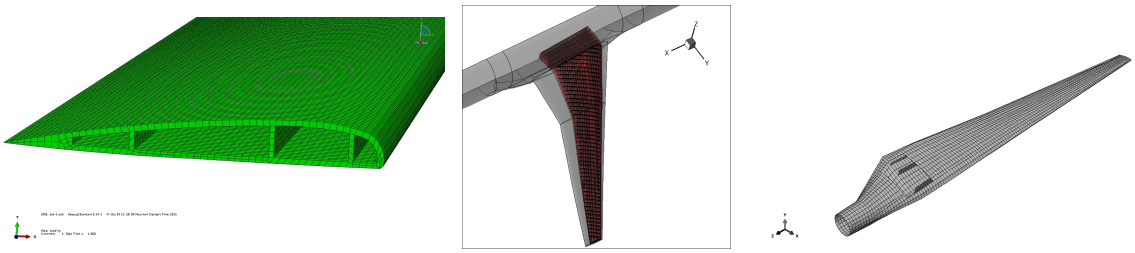

**Figure 2. (a) Brick-based structural model of HART2 rotor blade; (b) Shell-based model of CRM wing-box; (c) In-house constructed shell model of wind turbine blade**

.

## IV. FSI Formulation

In order to couple the computational structural dynamics (CSD) solver to the computational fluid dynamics (CFD) solver, a general fluid-structure interface (FSI) module has been developed. This interface is a stand-alone module that transfers the aerodynamic forces from the computational fluid dynamics (CFD) solver to the computational structural dynamics (CSD) model, and also returns the displacements generated from the CSD solver to the CFD surface mesh. The FSI must be capable of handling non-point matched overlapping CFD and CSD surface meshes of widely varying resolution and element types. Additionally, the FSI must be capable of handling CSD models that do not match the outer-mold line (OML) of the geometry used for the CFD surface mesh. This situation can arise either due to small differences in the geometry representation used for the CFD and CSD model, or due to an incomplete CSD model, for example in cases where only a portion of the complete structure is used in the CSD model, as is often the case in early design stages. In order to accommodate these different cases, the FSI represents the CFD surface mesh as a cloud of points, which enables a unified approach for structured and unstructured surface meshes. For each CFD surface point, the closest point on the surface of the CSD finite element mesh is found through a fast parallel search technique, which is based on the minimum distance search used for CFD turbulence model requirements.[35] Once all CFD surface points have been associated with their closest perpendicular projection on the CSD surface mesh, the CFD forces are transferred to the CSD surface nodes as:

$$\mathbf{F}_{CSD} = [T]\,\mathbf{F}_{CFD} \tag{1}$$

where [T] represents the rectangular transfer matrix which is computed assuming the surface CFD points are attached to their corresponding closest point on the surface CSD mesh via rigid links.[36] Conversely, the CSD displacements are transferred back to the CFD surface mesh as:

$$\mathbf{U}_{CFD} = [T]^T\,\mathbf{F}_{CSD} \tag{2}$$

By using the transpose of the force transfer matrix for the displacement transfer, the principle of conservation of virtual work is guaranteed.

To enhance robustness and increase flexibility, all CFD surface points and CSD surface faces are associated with a component number and the user can specify which CFD components should transfer forces to which CSD components. In this manner, specific components that do not contribute to loads on the flexible structure can be omitted. Figure 3 provides an illustration of the FSI applied to a standard aeroelastic test case, namely the High Reynolds Number Aerostructural Dynamics (HIRENASD) case.[37] This test case was the subject of the first Aeroelastic Prediction Workshop (AePW),[38] and various structural models and CFD grids are available for the HIRENASD geometry. In this case, we chose the fully hexahedral Nastran structural wing model available on the AePW web site, which is shown in Figure 3(a). This model is overlaid with the coarse unstructured mesh CFD grid, which contains 6.5 million grid points and is also available at the AePW web site. As documented on the web site, this structural model corresponds to one of the early models developed for the HIRENASD test case, and the model is known to not conform to the same OML as the CFD mesh. This is illustrated in Figure 4(a), and this model was purposely chosen to demonstrate the robustness of the current approach in dealing with inexact geometries. Additionally, the fairing/fuselage in the HIRENASD model which attaches to the wall is not flexible and does not transfer forces to the flexible wing as illustrated in Figure 4(b). This is handled in a natural manner with our component based FSI approach.

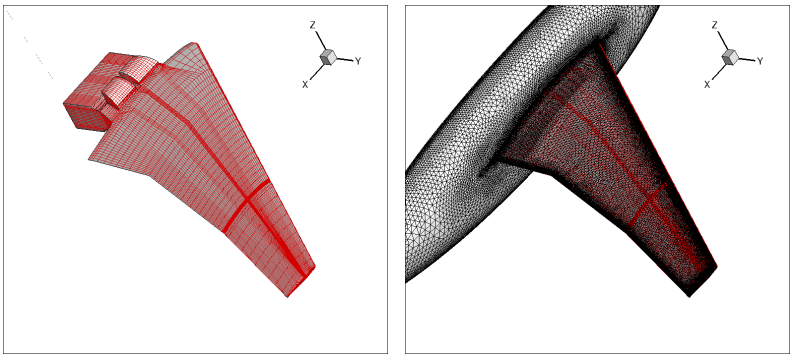

**Figure 3. HIRENASD aero-structural model; (a) Structural model based on 8-node incompatible mode hexahedral elements; (b) Structural model overlaid with unstructured CFD surface mesh.**

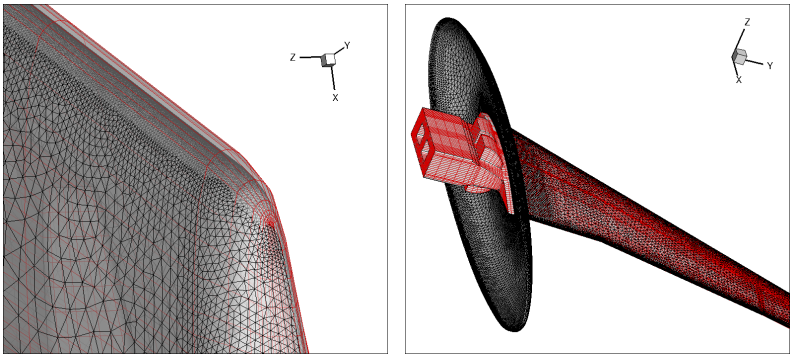

**Figure 4. HIRENASD aero-structural model; (a) Illustration of mismatch in wing tip leading edge area between structural model (red) and CFD model (black); (b) Illustration of rigid fuselage/fairing CFD component and internal structural model in region near wall.**

# V. Mesh Deformation

A mesh deformation capability is required in order to deform the unstructured CFD volume mesh in response to surface mesh displacements which occur throughout the simulation process. For aeroelastic problems, these surface displacements occur as a result of the surface deflections computed by the structural model in response to CFD computed aeroloads, which are transferred back to the CFD surface mesh through the FSI. Time dependent problems may also include prescribed surface deflections, such as those required for the simulation of the cyclic pitching of rotorcraft blades in forward flight. Finally, for shape optimization problems, design changes of the aerodynamic outer mold line must also be propagated into the interior CFD mesh. The mesh deformation approach adopted in this work is based on a linear elastic analogy whereby the unstructured CFD mesh is modeled as a linear elastic solid which deforms in response to prescribed surface deflections.[39] The modulus of elasticity of the mesh elements can be set either as inversely proportional to the cell volume, or as a function of the distance from the deflecting surface. On both cases, this results in stiff elements near the surface and more compliant elements away from the surface, thus preserving element shapes and avoiding negative volumes in regions near the deflecting surface. The mesh deformation equations are discretized using a second-order accurate continuous Galerkin finite-element approach, and the resulting equations are solved using the same parallel line-implicit multigrid algorithm employed for the flow solver. The adjoint of the mesh deformation equations has also been implemented and is solved in a similar fashion.

# VI. Results

## A. Structural Model

Several tests have been performed to both verify the implementation and validate the accuracy of the newly developed structural solver. A series of single element loading tests have been conducted for every element type developed thus far. An example is shown in Figure 5, where a single 4-node shell element is loaded on nodes 2 and 3 with a constant moment about the Y-axis, while nodes 1 and 4 are held fixed. Table 2 depicts the computed values of the rotational degrees of freedom of the four-node shell for this case. The agreement between the results of the current implementation and the Abaqus results, which is of the order of 8 significant figures, is typical of the agreement observed for all single element loading tests.

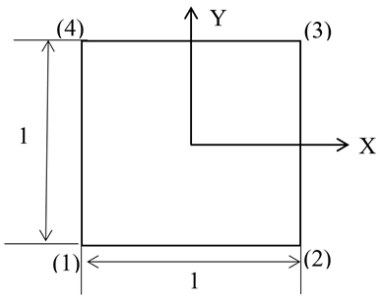


**Figure 5. Illustration of element test setup for verification of individual element formulation**

**Table 2. Comparison of nodal rotation results between in-house and Abaqus software for four-node shell element in bending**

| Node | $\theta_1$ (Current) | $\theta_1$ (Abaqus) | $\theta_2$ (Current) | $\theta_2$ (Abaqus) | $\theta_3$ (Current) | $\theta_3$ (Abaqus) |
|---|---|---|---|---|---|---|
| 1 | 1.20000004 | 1.20000001 | 0.00000000 | 0.00000000 | 0.00000000 | 0.00000000 |
| 2 | 1.20000004 | 1.20000001 | -12.00000004 | -12.00000001 | 0.00000000 | 0.00000000 |
| 3 | -1.20000004 | -1.20000001 | -12.00000004 | -12.00000001 | 0.00000000 | 0.00000000 |
| 4 | -1.20000004 | -1.20000001 | 0.00000000 | 0.00000000 | 0.00000000 | 0.00000000 |

In addition to single element tests, patch tests were conducted for incompatible mode elements and 4-node shell elements, in which a rectangular mesh of 5 distorted, trapezoidal-shaped elements is subjected to a loading which should produce a constant state of stress, as depicted in Figure 6. If the resulting distribution of stress is indeed uniform throughout all integration points, solution convergence with mesh refinement is ensured.[26] Tables 3 and 4 give patch test results with standard deviations for each component of stress.

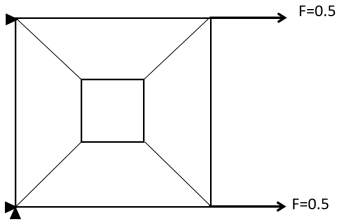


**Figure 6. Illustration of patch test for consistency of element formulation**

**Table 3. Patch test results for incompatible mode brick element. Standard deviations computed over values for all integration points.**

| Stress Component | Applied Stress | Standard Deviation From Applied Value |
|---|---|---|
| S11 | 1.0 | 8.041e-16 |
| S22 | 0.0 | 1.788e-16 |
| S33 | 0.0 | 1.717e-16 |
| S12 | 0.0 | 3.156e-16 |
| S13 | 0.0 | 1.272e-16 |
| S23 | 0.0 | 1.241e-16 |

**Table 4. Patch test results for 4-node shell element. Standard deviations computed over values for all integration points.**

| Stress Component | Applied Stress | Standard Deviation From Applied Value |
|---|---|---|
| S11 | 1.0 | 4.497e-16 |
| S22 | 0.0 | 1.498e-16 |
| S12 | 0.0 | 1.111e-16 |

Static deflection test cases using larger more complex structures have also been performed and the results have been validated against those produced by Abaqus. As an example, a NACA0012 square wing with cutout was modeled using 3570 incompatible mode hexahedral elements. In this case all displacements at the root are fixed, and the wing is subject to an evenly distributed body force in the Z-direction. The computed S22 stresses are depicted in Figure 7, while the maximu values of stresses, strains and displacements computed using the in-house code are compared with those produced by Abaqus in Table 5. As seen from the tabulated results, the differences between the in-house code and Abaqus are well below 1% for all quantities.

In order to validate the structural dynamic modelling capability and the Newmark Beta time-integration scheme, a free vibration test is simulated using the fully hexahedral HIRENASD wing model described previously. The model consists of approximately 42,000 hexahedral elements which are treated as 8-node incompatible mode hex elements (CD38I in Abaqus notation). The structural model is initialized with zero nodal displacements and accelerations, but with a nodal velocity distribution corresponding to the wing first

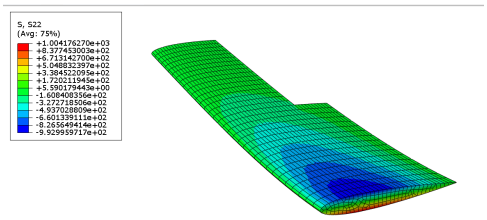

**Figure 7. Computed stresses for NACA0012 wing test case**

**Table 5. Comparison between computed maximum displacements, stresses and strains using in-house code and Abaqus for NACA0012 wing test case.**

| | Current | Abaqus | % Error |
|---|---|---|---|
| Max U3 | 1.04400916E-01 | 1.03656776E-01 | 0.7153 % |
| Max S2 | 1.00458404E+01 | 1.00417627E+03 | 0.0406 % |
| Max E2 | 9.82259953E-04 | 9.81980236E-04 | 0.0285 % |

bending mode as shown in Figure 8. The Newmark Beta time integration scheme is employed with a time step corresponding to 1/100 of the period of the natural frequency of the wing in its first bending mode. The natural vibration frequency is computed as 26.55 Hz, which is consistent with the results produced by Abaqus and very close to the value of 26.53 reported for this model on the AePW web site.[40]

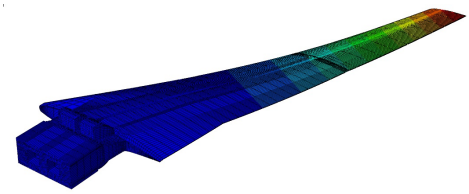

**Figure 8. Illustration of initial velocities based on first bending mode for the HIRENASD free vibration test case**

In addition to the Newmark Beta time integration scheme, the time-spectral approach has also been implemented for purely periodic structural problems as described above. For this case, a shell model of the Hart2 rotorcraft blade structure has been created as shown in Figure 9(a). This blade model is subjected to a periodic tip forcing, given as $F(t) = sin(t) + 2sin(2t) + 3sin(3t)$. Note that the lowest forcing harmonic corresponds to roughly twice the natural frequency of the first bending mode of the blade, which was calculated as 0.083Hz. Figure 9(b) depicts the blade response in terms of the displacement at the tip location where the force is applied using both the Newmark Beta time integration scheme with 40 time steps per period, and the time-spectral approach using 7 time instances within a single period, which is the minimum number required to capture this periodic forcing which contains 3 harmonics. The time spectral solution converges to the periodic solution without the need to compute the initial transients, as seen in Figure 9. In the fully periodic response region, the Newmark Beta and time-spectral solutions are nearly indistinguishable.

In order to verify the adjoint sensitivity implementation, a test case was constructed using a beam model with ten 8-node brick elements arranged single file in the z-direction, subjected to an end load while clamped on the opposite end, resulting in a nodal transverse displacement, $u_{nodal}$ (z). The stiffness (elastic modulus) of the beam was chosen as the sole design variable, with an objective transverse displacement of

$$u_{obj} = 4.10^{-5} z^2 \tag{3}$$

which leads to the objective functional

$$L(u) = \sum_{i=1}^{n} \left(u_{nodal} - u_{obj}\right)_i \tag{4}$$

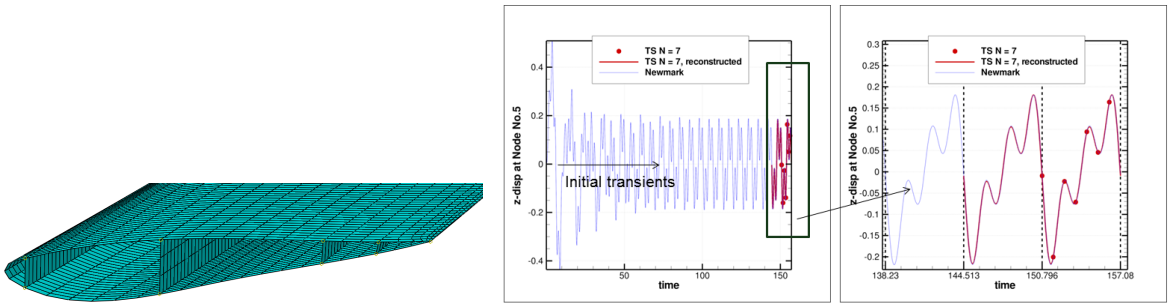


**Figure 9. (a) Partial view of shell model for HART2 blade structurel (b) Comparison of free vibration displacement time history computed using Newmark Beta time integration scheme with 40 time steps per period and time-spectral approach with 7 time instances per period.**

where n represents the number of nodes. The derivative of the objective function with respect to the modulus of the beam in the initial configuration was computed using the adjoint method, as well as the forward sensitivity or tangent method, the complex step method, and a regular finite difference approach. The same test was then repeated using the cross-sectional dimension of the bar as the design variable instead of the modulus. The results in Table 6 were obtained, showing machine precision agreement between the adjoint and tangent implementations, and 6 to 8 digits of agreement with respect to the complex step implementation.

**Table 6. Verification of adjoint sensitivities for 10 element beam test case**

| Design Variable : D | Adjoint | Tangent | Complex | Finite Difference |
|---|---|---|---|---|
| Elastic Modulus | 6.550578258613791e-5 | 6.550578258613**788**e-5 | 6.55057825**9653104**e-5 | 6.55057**9473388012**e-5 |
| Cross Section | 2.176429767520180e-4 | 2.176429767520**195**e-4 | 2.1764**26554551170**e-4 | 2.1764**34086331999**e-4 |

To further validate the structural adjoint sensitivity implementation, a full optimization has been performed on a shell model of the Hart-2 rotor blade, shown in Figure 10. In this test, a distributed body force was applied to the blade in the upward direction, while the blade was clamped at the root. Then using the adjoint driven optimization procedure, the stiffness (Youngs modulus) along the length of the blade was modified to conform the deformation to a certain target function, given as

$$u_{obj} = 5.10^{-3}(y - 3.75)^2 \tag{5}$$

The blade was divided into ten equal segments along its length, and each segments stiffness was defined as a design variable. The objective function was defined as in equation (4) and the optimization was performed using a modified conjugate gradient algorithm. Figure 11 shows the evolution of the HART2 blade deflection to the target shape though progressive optimization steps as well as the overall convergence of the optimization process in terms of reduction of the objective functional and norm of the sensitivity vector.

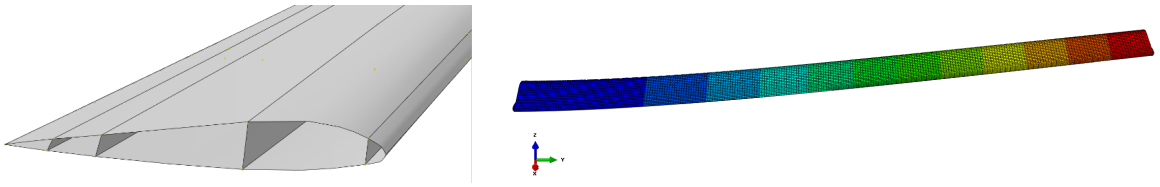

**Figure 10. (a) Cross-sectional view of shell-based model of HART2 rotor blade; (b) Initial transverse deflection of HART2 rotor blade under transverse loading for optimization problem**

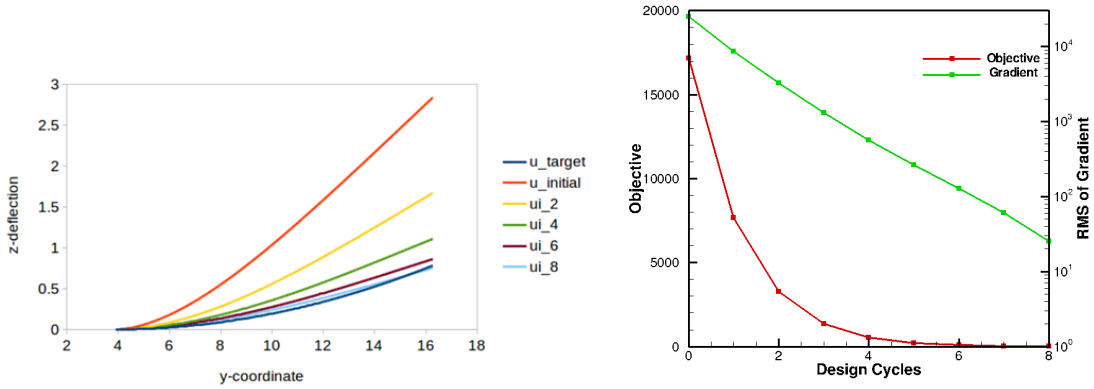


**Figure 11. (a) Evolution of blade shape with optimization steps versus target shape; (b) Convergence history of structural optimization problem in terms of objective and norm of sensitivity vector**

## B. Aero-Structural Results

Initial validation of the combined CFD, CSD and FSI components has been performed by computing a static aeroelastic case using the HIRENASD test case. The flow conditions include Mach=0.8, Incidence = 1.5 degrees, Re=7 million and a dynamic pressure (q) of 40,055.4 Pa. The structural model consists of the fully hexahedral NASTRAN brick model available on the AePW web site. This model contains a total of approximately 42,000 elements. The hexahedral elements were interpreted as 8-node hex incompatible mode elements (CD38I designation in Abaqus). The CFD mesh corresponds to the coarse node-centered unstructured mesh available at the AePW web site, which contains a mixture of prismatic and tetrahedral elements with approximately 6.5 million points. The flow solver is run a total of 3 fluid structure coupling cycles. Within each coupling cycle, the flow solver is run 200 multigrid cycles, the CFD forces are transferred to the structural model which is solved by direct inversion, and the displacements are returned to the surface CFD mesh. The mesh deformation solver is then run for 50 multigrid cycles, and the process is repeated. Figure 12 illustrates the convergence of the CFD solver for this case, showing diminishing jumps in convergence at each fluid-structure update. The flexible wing lift coefficient is computed as 0.3304, which compares well with the values reported in the AePW workshop for the static aeroelastic case using modal analysis.[38] The computed surface pressure profile and the distribution of static deflection vertical displacements are shown in Figure 12.

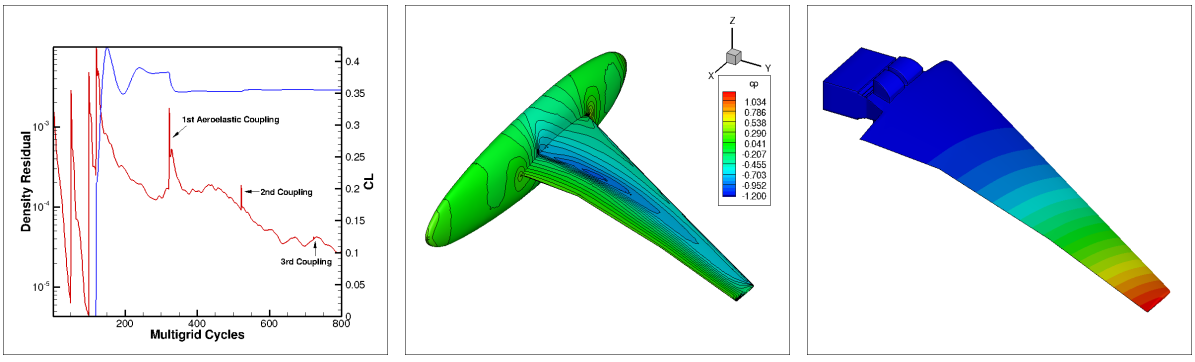


**Figure 12. (a) Convergence history of static aeroelastic HIRENASD case; (b) Computed surface pressure coefficient contours on final flexible wing solution; (c) Computed displacement field on flexible wing structure.**

A time-dependent aeroelastic case is formulated using the same HIRENASD structural model and CFD mesh. Using the same flow conditions, the flow is first computed with the wing structure held fixed (i.e. rigid wing with no allowed displacements). At time t=0, the wing is suddenly released and responds to the airloads with a periodic motion with decreasing amplitude which eventually converges to the previously

computed steady-state aeroelastic solution. A time step size corresponding to 0.01 of the period of the natural frequency of the first bending mode of the wing is used in this calculation. Figure 13(a) depicts the time response of the wing, as a plot of the displacement of a point near the wing tip. Figure 13(b) illustrates the convergence of the coupled dynamic aeroelastic system, while Figure 13(c) depicts the convergence history of the mesh deformation equations. A total of 3 coupling cycles is used at each time step, with 10 multigrid cycles employed for the CFD solver within each coupling cycle, resulting in a total of 30 flow cycles per time step. The jumps in residual and lift at the start of each coupling cycle are seen to decrease monotonically and the lift values at the end of each time step are well converged. The mesh deformation equations are converged 10 orders of magnitude at each coupling iteration. Since these equations are initialized with the displacements obtained from the previous coupling cycle, the initial residuals at each coupling iteration decrease monotonically, indicating that the deflections of the structural model are converging as the fully coupled aeroelastic problem is solved to tighter tolerances. This problem was run on 128 processors and required approximately 1 minute for each physical time step.

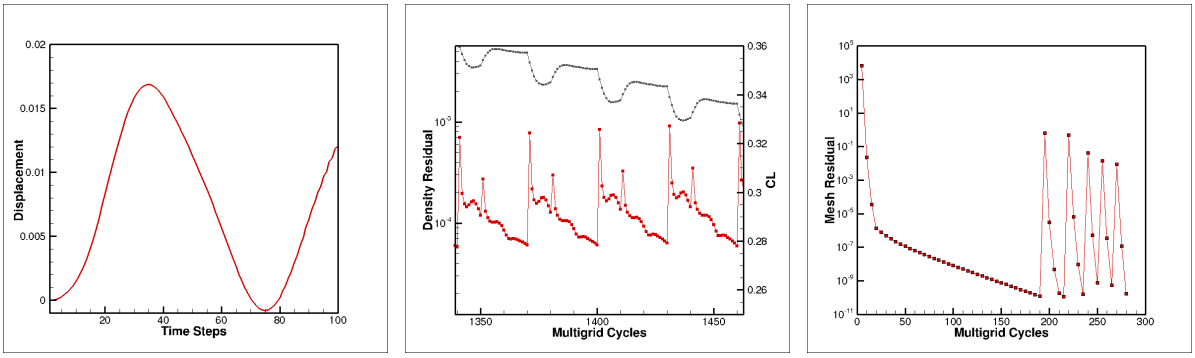


**Figure 13. (a) Time history of tip displacement for dynamic aeroelastic HIRENASD test case; (b) Convergence history over selected time steps for flow solver; (c) Convergence history of mesh deformation problem at selected time steps**

(c)

## VII. Conclusions and Future Work

This paper describes work towards the development of a high fidelity aerostructural analysis and design capability for time dependent problems. All components of the aeroelastic capability have been validated independently, both for analysis and for adjoint sensitivity computations. The coupled aeroelastic analysis capability has been demonstrated for steady state and time dependent problems. In future work, the fully coupled adjoint capability will be demonstrated for time dependent problems and used to perform gradient-based optimization using both aerodynamic shape and structural design variables. Additionally, the time-spectral approach for periodic problems, which has been demonstrated for both aerodynamic and structural dynamic problems independently, will be applied to the coupled aeroelastic problem.

## VIII. Aknowledgements

This work has been funded by AFOSR STTR contract FA9550-14C-0035. Computational resources have been provided by the University of Wyoming Advanced Research Computing Center (ARCC) and by the NCAR-Wyoming Supercomputer Center (NWSC). We also wish to aknowledge the derivation of the second order time-spectral coefficients performed and provided by B. Roget.

## References

[1]Vassberg, J. C., Tinoco, E. N., Mani, M., Zickuhr, T., Levy, D., Brodersen, O. P., Eisfeld, B., Wahls, R. A., Morrison, J. H., Mavriplis, D. J., and Murayama, M., "Summary of the Fourth AIAA CFD Drag Prediction Workshop," AIAA Paper 2010-4547.

[2]Wissink, A., Jayaraman, B., Datta, A., Sitaraman, J., Potsdam, M., Kamkar, S., Mavriplis, D., Yang, Z., Jain, R., Lim,

J., and Strawn, R., "Capability Enhancements in Version 3 of the HELIOS High Fidelity Rotorcraft Simulation Code," AIAA Paper 2012-713, Presented at the 50th AIAA Aerospace Sciences Meeting and Exhibit, Nashville TN.

[3] "Third AIAA Drag Prediction Workshop." San Francisco, CA. http://aaac.larc.nasa.gov/tsab/cfdlarc/aiaa-dpw.

[4] Jameson, A., "Aerodynamic Shape Optimization using the Adjoint Method," VKI Lecture Series on Aerodynamic Drag Prediction and Reduction, von Karman Institute of Fluid Dynamics, Rhode St Genese, Belgium.

[5] Reuther, J. J., Alonso, J. J., Martins, J. R. R. A., and Smith, S. C., "A coupled aero-structural optimization method for complete aircraft configurations," AIAA Paper 97-187, 37th Aerospace Sciences Meeting, Reno, NV.

[6] Maute, K., Nikbay, M., and Farhat, C., "Coupled analytical sensitivity analysis and optimization of three-dimensional nonlinear aeroelastic systems," *AIAA journal*, Vol. 39, No. 11, 2001, pp. 2051–2061.

[7] Kenway, G. and Martins, J. R. R. A., "Multipoint High-Fidelity Aerostructural Optimization of a Transport Aircraft Configuration," *Journal of Aircraft*, Vol. 51, No. 1, 2014, pp. 144–160.

[8] Mani, K. and Mavriplis, D. J., "An Unsteady Discrete Adjoint Formulation for Two-Dimensional Flow Problems with Deforming Meshes," *AIAA Journal*, Vol. 46, No. 6, 2008, pp. 1351–1364.

[9] K. Mani, B. L. and Mavriplis, D., "Adjoint-Based Unsteady Airfoil Design Optimization with Application to Dynamic Stall," Paper presented at AHS Forum 68, Fort Worth TX.

[10] Mavriplis, D. J., "Solution of the Unsteady Discrete Adjoint for Three- Dimensional Problems on Dynamically Deforming Unstructured Meshes," AIAA Paper 2008-0727, 46th Aerospace Sciences Meeting, Reno NV.

[11] Nielsen, E. J., Diskin, B., and Yamaleev, N. K., "Discrete Adjoint-Based Design Optimization of Unsteady Turbulent Flows on Dynamic Unstructured Grids," *AIAA Journal*, Vol. 48, 2010, pp. 1925–1206, doi:10.2514/1.J050035.

[12] Nielsen, E. J. and Diskin, B., "Discrete adjoint-based design for unsteady turbulent flows on dynamic overset unstructured grids," *AIAA journal*, Vol. 51, No. 6, 2013, pp. 1355–1373.

[13] Jones, W. T., Nielsen, E. J., Lee-Rausch, E. M., and Acree, C. W., "Multi-point Adjoint-Based Design of Tilt-Rotors in a Noninertial Reference Frame," AIAA Paper 2014-0290, 10th AIAA Multidisciplinary Design Optimization Conference.

[14] Mani, K. and Mavriplis, D. J., "Geometry Optimization in Three-Dimensional Unsteady Flow Problems using the Discrete Adjoint," AIAA Paper 2013-0662, 51st Aerospace Sciences Meeting, Grapevine TX.

[15] Mani, K. and Mavriplis, D. J., "Adjoint Based Sensitivity Formulation for Fully Coupled Unsteady Aeroelasticity Problems," *AIAA Journal*, Vol. 47, No. 8, 2009, pp. 1902–1915.

[16] Mishra, A., Mani, K., Mavriplis, D. J., and Sitaraman, J., "Time Dependent Adjoint-based Optimization for Coupled Aeroelastic Problems," AIAA Paper 2013-2906, Presented at the 21st AIAA CFD Conference, San Diego, CA.

[17] Mishra, A., Mani, K., Mavriplis, D. J., and Sitaraman, J., "Time-dependent Adjoint-based Aerodynamic Shape Optimization Applied to Helicopter Rotors," *70th American Helicopter Society Annual Forum, Montreal, QC, CA*, May 20–22 2014.

[18] Mishra, A., Mavriplis, D. J., and Sitaraman, J., "Time-dependent Aero-elastic Adjoint-based Aerodynamic Shape Optimization of Helicopter Rotors in Forward Flight," AIAA Paper 2015-1130, 56th AIAA Aerospace Sciences Meeting, Kissimmee, FL.

[19] Vassberg, J. C., Tinoco, E. N., Mani, M., Brodersen, O. P., Eisfeld, B., Wahls, R. A., Morrison, J. H., Zickuhr, T., Laflin, K. R., and Mavriplis, D. J., "Abridged Summary of the Third AIAA Computational Fluid Dynamics Drag Prediction Workshop," *Journal of Aircraft*, Vol. 45, No. 3, 2008, pp. 781–798.

[20] Mavrplis, D. J., Long, M., Lake, T., and Langlois, M., "NSU3D Results for the second AIAA High-Lift Prediction Workshop," AIAA Paper 2014-748, 52nd Aerospace Sciences Meeting, National Harbor, MD.

[21] Mavriplis, D. J., Z.Yang, and Long, M., "Results using NSU3D for the First AIAA Aeroelastic Prediction Workshop," AIAA Paper 2013-0786, 51st AIAA Aerospace Sciences Meeting, Grapevine TX.

[22] Mavriplis, D. J. and Mani, K., "Unstructured Mesh Solution Techniques using the NSU3D Solver," AIAA Paper 2014-081, 52nd Aerospace Sciences Meeting, National Harbor, MD.

[23] Mavriplis, D. J. and Yang, Z., "Time Spectral Method for Periodic and Quasi-Periodic Unsteady Computations on Unstructured Meshes," *Mathematical Modeling of Natural Phenomena*, Vol. 6, No. 3, May 2011, pp. 213–236, DOI: http://dx.doi.org/10.1051/mmnp/20116309.

[24] Lyness, J. N., "Numerical Algorithms based on the Theory of Complex Variables," Proceedings ACM 22nd National Conference, Thomas Book Company, Washington DC.

[25] Martins, J., Sturdza, P., and Alonso, J., "The complex-step derivative approximation," *ACM Transactions on Mathematical Software (TOMS)*, Vol. 29, No. 3, 2003, pp. 245–262.

[26] Bathe, K.-J., *Finite element procedures*, Klaus-Jurgen Bathe, 2006.

[27] Cheney, W. and Kincaid, D., *Numerical Mathematics and Computing, 6th Edition*, Thomson Brooks/Cole, 2008.

[28] Sloan, S. W., "A FORTRAN program for profile and wavefront reduction," *International Journal for Numerical Methods in Engineering*, Vol. 28, No. 11, 1989, pp. 2651–2679.

[29] Amestoy, P. R., Duff, I. S., LExcellent, J.-Y., and Koster, J., "MUMPS: a general purpose distributed memory sparse solver," *Applied Parallel Computing. New Paradigms for HPC in Industry and Academia*, Springer, 2001, pp. 121–130.

[30] Krysl, P., Lall, S., and Marsden, J., "Dimensional model reduction in non-linear finite element dynamics of solids and structures," *International Journal for numerical methods in engineering*, Vol. 51, No. 4, 2001, pp. 479–504.

[31] Roget, B., "Personal communication," May, 2014.

[32] Ekici, K. and Hall, K., "Nonlinear Analysis of Unsteady Flows in Multistage Turbomachines using Harmonic Balance," *AIAA Journal*, Vol. 45, No. 5, 2007, pp. 1047–1057.

[33] Leffell, J., Murman, S., and Pulliam, T., "An Extension of the Time-Spectral Method to Overset Solvers," AIAA Paper 2013-637, Presented at the 51st AIAA Aerospace Sciences Meeting, Grapevine TX.

[34] Mundis, N. and Mavriplis, D., "Toward an Optimal Solver for Time-spectral Solutions on Unstructured Meshes," AIAA Paper 2016-xxxx, Presented at the 54rd AIAA Aerospace Sciences Conference, San Diego CA.

[35]Roget, B. and Sitaraman, J., "Wall distance search algorithm using voxelized marching spheres," *Journal of Computational Physics*, Vol. 24, 2013, pp. 76–94.

[36]Martins, J. R. R. A., Alonso, J. J., and Reuther, J. J., "A coupled-adjoint sensitivity analysis method for high-fidelity aero-structural design," *Optimization and Engineering*, Vol. 6, No. 1, 2005, pp. 33–62.

[37]Reimer, L., Boucke, A., Ballmann, J., and Behr, M., "Computational Analysis of High-Reynolds Number Aero-structural dynamics HIRENASD," Proc. of the International Forum on Aeroelasticity and Structural Dynamics (IFASD) 2009, Paper IFASD-2009-130.

[38]Heeg, J., Chwalowski, P., Florance, J., Wieseman, C., Schuster, D., and Perry III, B., "Overview of the Aeroelastic Prediction Workshop," AIAA Paper 2013-783, 51st Aerospace Sciences Meeting, Grapevine, TX.

[39]Yang, Z. and Mavriplis, D. J., "A Mesh Deformation Strategy Optimized by the Adjoint Method on Unstructured Meshes," *AIAA Journal*, Vol. 45, No. 12, 2007, pp. 2885–2896.

[40] "First Aeroelastic Prediction Workshop," https://c3.nasa.gov/dashlink/static/media/other/AEPW.htm.